Journal of Superconductivity and Novel Magnetism (2019) 32:1057–1065
https://doi.org/10.1007/s10948-018-4793-6

ORIGINAL PAPER

Microstructural, Optical, and Magnetic Properties of Vanadium-Substituted Nickel Spinel Nanoferrites

A. D. Korkmaz[1] · S. Güner[2] · Y. Slimani[3] · H. Gungunes[4] · Md. Amir[5] · A. Manikandan[6] · A. Baykal[7]

Received: 24 June 2018 / Accepted: 27 June 2018 / Published online: 11 July 2018

Abstract

The current study investigates the impact of vanadium substitution on the structural, magnetic, and optical properties of $NiFe_{2-x}V_xO_4$ ($x \leq 0.3$) nanoparticles (NPs) produced by the cost-effective sol-gel route. The as-prepared spinel ceramic powders were examined by X-ray diffraction (XRD), UV-visible diffuse reflectance spectroscopy (DRS), Fourier transform infrared (FT-IR) spectroscopy, scanning electron microscopy (SEM), and vibrating sample magnetometry (VSM). The functional groups, spinel phase, and crystal structure were confirmed by XRD and FT-IR, respectively. The crystallites size decreased from 45.24 to 36.56 nm as the doping process increases. The plots of Tauc were drawn to determine optical band gap magnitudes of 1.291, 1.302, and 1.312 eV for $x = 0.0$, 0.2, and 0.3, respectively. The estimated saturation magnetization is maximum for pristine $NiFe_2O_4$ NPs and decreases to minimum for $NiFe_{1.7}V_{0.3}O_4$ NPs. The σ-H hysteresis loops have finite coercivity (between 125 and 169 Oe) and retentivity (between 9.36 and 14.04 emu/g) values. The calculated σ_r/σ_s ratios are lower than 0.500, assigning the uniaxial anisotropy for $NiFe_{2-x}V_xO_4$. The effective anisotropy constants (K_{eff}) are in the range of 0.824×10^5 and 1.303×10^5 Erg/g. The magnetocrystalline anisotropy field (H_a) values are around 5.0 kOe. The characteristics of hysteresis (σ-H) curves and the order of magnetic data reveal the soft ferrimagnetic feature of as-prepared nanoparticle samples. From Mossbauer analysis, the variations in hyperfine magnetic field, quadrupole splitting, line width, and isomer shift have been evaluated. The distribution of cations showed that the octahedral B sites are occupied by all the ions of V^{3+}. Mossbauer spectra are composed of four Zeeman sextets and one doublet.

Keywords Vanadium substitution · Nickel ferrites · Magnetic properties · Mossbauer spectroscopy · Optical properties · Cation distribution

1 Introduction

Magnetic nanoparticles (MNPs) are used in a wide area of advanced scientific research due to their potential applications in several fields such as catalysis, wastewater treatment, microwave devices, and magnetic pigments as well as in biomedical applications, for example in magnetic resonance imaging (MRI) and cancer therapy [1–5]. Cubic spinel ferrites, MFe_2O_4 (M = Fe^{2+}, Cu^{2+}, Zn^{2+}, etc.), are well known as one of the significantly studied magnetic nanomaterials [6]. They crystallize in a cubic crystal structure and Fd3m space group. The unit

✉ Y. Slimani
yaslimani@iau.edu.sa; slimaniyassine18@gmail.com

1 Department of Chemistry, Istanbul Medeniyet University, Uskudar, 34700 Istanbul, Turkey

2 Institute of Inorganic Chemistry, RWTH Aachen University, Landoltweg 1, 52074 Aachen, Germany

3 Department of Biophysics, Institute for Research and Medical Consultations (IRMC), Imam Abdulrahman Bin Faisal University, P.O. Box 1982, Dammam 31441, Saudi Arabia

4 Department of Physics, Hitit University, Çevre Yolu Bulvarı, 19030 Çorum, Turkey

5 Instrument Design and Development Centre (IDDC), Indian Institute of Technology Delhi, Hauz Khas, New Delhi 110016, India

6 Department of Chemistry, Bharath Institute of Higher Education and Research (BIHER), Bharath University, Chennai, Tamil Nadu 600073, India

7 Department of Nano-Medicine Research, Institute for Research and Medical Consultations (IRMC), Imam Abdulrahman Bin Faisal University, P.O. Box 1982, Dammam 31441, Saudi Arabia

cell includes 8 formula units with four metal cations and 32 oxygen ions that are distributed in various two types of non-equivalent interstitial sites: 64 tetrahedral (A) and 32 octahedral (B) sites where four and six oxygen ions surround metal cations, respectively [7, 8]. The spinel MFe_2O_4 adopts one of the three kinds of the structure: inverse, normal, or mixed cubic spinel structure. The bulk- and nano-sized $NiFe_2O_4$ have an inverse spinel structure (8 Ni^{2+} are distributed in B sites, while 16 Fe^{3+} occupied equally the A and B sites) [9, 10]. Some studies have reported that Ni ferrite nanoparticles (NPs) smaller than a few nanometers exhibit a mixed structure [11]. Ni ferrite is expressed as $\left(Ni_{1-i}^{2+}Fe_i^{3+}\right)_A\left(Ni_i^{2+}Fe_{2-i}^{3+}\right)_B O_4$ where i refers to the inversion grade (the mixed spinel, $0 < i < 1$). A synthesis situation may influence the degree of inversion [12]. Due to the large magnetic moment and magneto-optic and magneto-electric effects, $NiFe_2O_4$ NPs are considered an important member of $NiFe_2O_4$ inverse spinel ferrites with the ferrimagnetic type and exhibit interesting magnetic properties compared to their corresponding bulk compounds [13]. The chemical manipulation of spinel soft ferrites plays a key role to control properties of the structure. Recently, the researchers have shown that the vanadium-substituted and vanadium-doped ferrites have an interesting impact on the magnetic properties and crystallographic of the soft ferrites [14]. $CoFe_{2-1.67x}V_xO_4$ ($x = 0.1$ and 0.2) and $CoFe_{2-x}V_xO_4$ ($0 < x < 0.25$) were fabricated by Heiba et al. [15] via the sol-gel method. They found that the vanadium in $CoFe_{2-1.67x}V_xO_4$ samples was distributed equally between A and B sites. Furthermore, due to ionic size mismatch between cations, when the concentration of vanadium increases, the microstrain grows markedly. However, pure $CoFe_2O_4$ has a saturation magnetization higher than the samples with V substitution; the amount of Co^{2+} cations in the tetrahedral site influences on the magnetocrystalline anisotropy, and this results in altering the coercive field with an increasing amount of V [15]. Maisnam et al. [16] displayed that the porosity and grain size of the $Li_{0.5+t}Co_{0.2}Ti_{0.2}V_tFe_{2.1-2t}O_4$ initially grow and then reduce when the concentration of vanadium increases up to $t = 0.1$, while with rising vanadium concentration, the saturation magnetization and Curie temperature decreased. The melting point of V_2O_5 is low (670 °C), and when it is in a liquid phase, it increases sintering on the grain boundaries. However, during prolonged sintering, it evaporates and makes the grain boundaries of the ferrite without a significant increase of a V_2O_5-rich phase [17]. Moreover, the sintering temperature and increasing densification with grain growth decrease when doping of V_2O_5 to some ferrite systems, like Mn-Zn ferrite, Li ferrite, and Ni-Cu-Zn ferrite [18]. Jain et al. [19] studied the impact of V_2O_5 inclusion on electrical and magnetic properties of Ni-Zn ferrites.

In the present study, the new uniaxial anisotropy magnetic $NiFe_{2-x}V_xO_4$ NPs ($0.0 \leq x \leq 0.3$) were produced through a cost-effective sol-gel route, and to our knowledge, their structural, magnetic, Mossbauer, and optical characterizations were presented for the first time.

2 Experimental Procedures

2.1 Synthesis Details

Sol-gel technique has been employed for the preparation of $NiFe_{2-x}V_xO_4$ ($x \leq 0.3$) NPs. Iron(III) nitrate ($Fe(NO_3)_3$), nickel(II) nitrate hexahydrate ($Ni(NO_3)_2{\cdot}6H_2O$), and ammonium metavanadate (NH_4VO_3) were dissolved in stoichiometric amounts in distilled water (50 mL) where 2 g of citric acid was as employed as fuel. Then, 30% ammonia solution was added to the mixture drop by drop to regulate the pH at 7. The solution was heated till 80 °C under continuous stirring and kept at this temperature for 7 h. After cooling to room temperature (RT), the sample was collected by magnetic separation with the aid of a permanent magnet. Finally, the sample was grinded and annealed at 1000 °C for 6 h. The above procedure was repeated for $x = 0.0$, 0.2, and 0.3 substitutions.

The structure was examined by X-ray diffraction (XRD; Rigaku D/Max-IIIC) with Cu α radiationand Fourier transform infrared (FT-IR) spectrometry (ATR Bruker α-P). The morphology was confirmed via JEOL JSM-6490 scanning electron microscopy (SEM) coupled with EDXS. The percent diffuse reflectance (%DR) was studied via a Thermo Scientific Evolution 300 PC model spectrophotometer along with Praying Mantis Diffuse Reflectance Accessory. The magnetic properties were carried out by vibrating sample magnetometer (VSM) (BHV-50 of Riken Danish Company). The Mössbauer spectra was carried out using a spectrometer working with the use of 25 mCi ^{57}Co (Rh matrix).

3 Results and Discussions

3.1 Structure Examination

The XRD patterns of $NiFe_{2-x}V_xO_4$ ($x \leq 0.3$) NPs are depicted in Fig. 1 and confirm that the various fabricated samples are singlephase spinel ferrite. Bragg reflections were indexed to $NiFe_2O_4$ (JCPDS File no. 10-0325) of the space group Fd3m [20, 21]. No any peak of impurity or intermediate phases (NiO or Fe_2O_3) is observed. The results of Rietveld refinement are summarized in Table 1. The crystallite sizes are determined from the XRD pattern by the

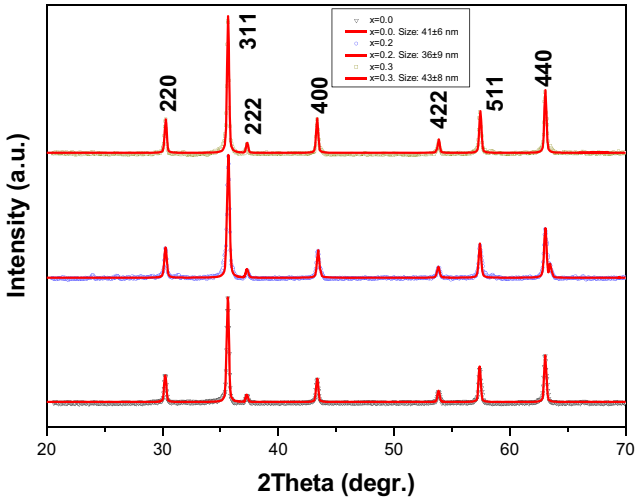

Fig. 1 Powder XRD patterns of $NiFe_{2-x}V_xO_4$ ($x \leq 0.3$) NPs

line profile fitting method by means of (1) in references [22] and [23] (Table 1). The lattice parameter goes on increasing from 8.3248 to 8.3455 Å with increasing x. The increase of a_0 with x linearly was due to the replacement of Fe^{3+} (0.67 Å) by V^{3+} (0.78 Å).

3.2 Spectral Analysis

The results of spectral analysis of $NiFe_{2-x}V_xO_4$ ($x \leq 0.3$) NPs are depicted in Fig. 2. It is known that two main metal-oxygen bands caused by the vibrations at the O_h site (ν_1) occurred in the frequency 430–385 cm^{-1} range, and those caused by the vibrations at the T_d site (ν_2) occurred in the frequency 600–500 cm^{-1} range which appear in spinel ferrite systems [24]. In this study, the symmetrical stretching vibrations of Fe-O band at the t_d site are detected at around 550 cm^{-1} [24]. Due to the shorter M–O bond length in the T_d site than that in the O_h site, the T_d stretching vibrations are observed at a higher wavenumber in comparison to the O_h stretching vibrations [25], and because of the spectral resolution of our FT-IR device, it was not possible to observe the peak below 450 cm^{-1}.

Table 1 Structural parameters for $NiFe_{2-x}V_xO_4$ ($x \leq 0.3$) NPs with space group Fd3m (single-phase cubic spinel structure of $NiFe_2O_4$ NPs)

x	D (nm)	a_0 (Å)
0.0	45.24	8.3248
0.2	39.85	8.3312
0.3	36.56	8.3455

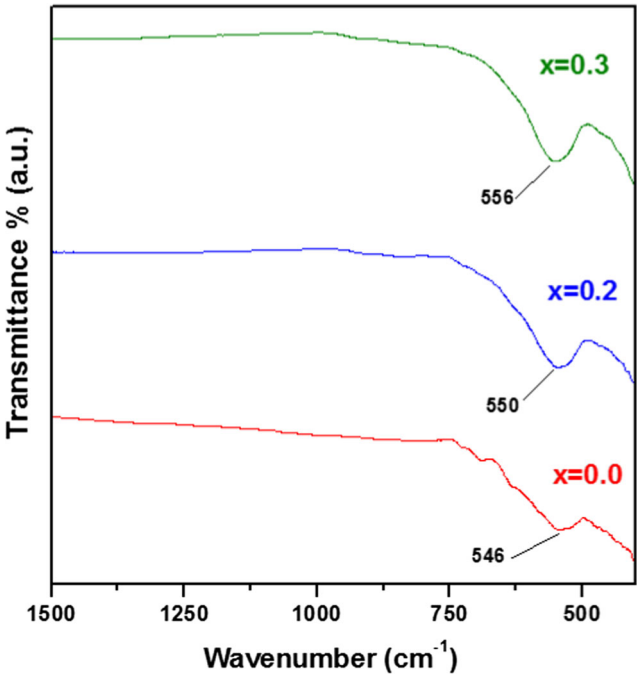

Fig. 2 FT-IR spectra of $NiFe_{2-x}V_xO_4$ ($x \leq 0.3$) NPs

3.3 Morphological Analysis

Figure 3a, b shows the SEM images, elemental mapping, and EDX spectra of $NiFe_2O_4$ ($x = 0.0$) and $NiFe_{1.7}V_{0.3}O_4$ ($x = 0.3$) NPs, respectively. The average grain size is around 150 nm for each product. The final samples exhibit fluffy, porous, and sponge-like structure, which is a consequence of the generation of substantial amounts of gas in the autocombustion approach. As the ratio of the vanadium substitution increases, the structure becomes less porous. This can be explained by the lower melting point (670 °C) of vanadium; as the vanadium amount increases, it affects the microstructure by densification [26]. The existence of V in uniaxial $NiFe_2O_4$ NPs is demonstrated by the elemental mapping and EDX spectra in Fig. 4a, b, respectively. The EDX spectra confirmed that products consist of V, Ni, Fe, and O elements, and no other elements were observed which confirmed the purity of the sample.

3.4 Optical Properties

Optical analyses were based on %DR measurements. The spectra are collected for different products in the 200–800 nm wavelength range of light. The recorded spectra are given in Fig. 5. All samples absorb at least 75% of the light along the sweep range. The electrons in the valence band absorb energy and jump to the conduction band upon the exposure of the powder samples to light. The difference between those bands is called as the optical energy band gap

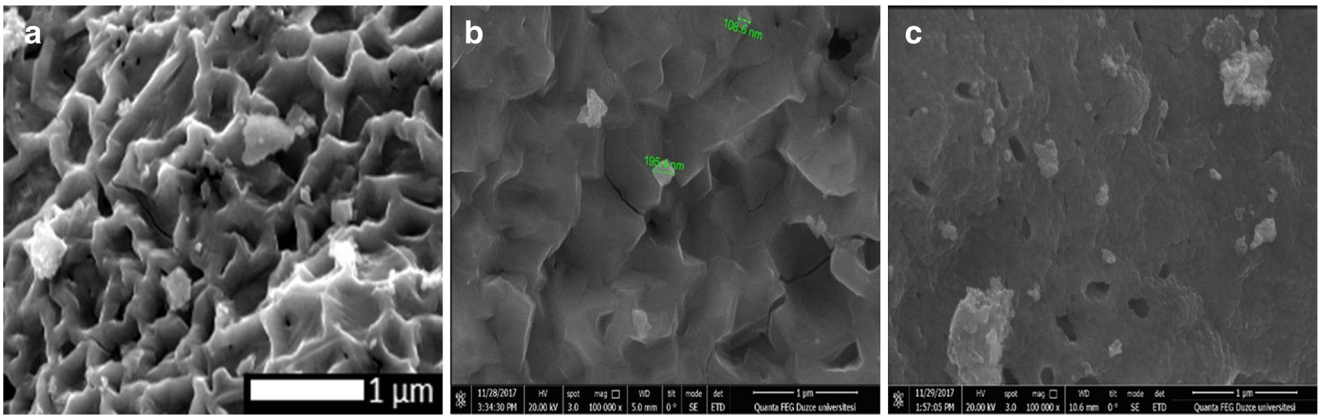

Fig. 3 SEM micrographs of $NiFe_{2-x}V_xO_4$ NPs. **a** $x = 0.0$. **b** $x = 0.2$. **c** $x = 0.3$

(E_g) and can be estimated from the known Tauc equation [27–29]

$$\alpha h\upsilon = A(h\upsilon - E_g)^n \quad (1)$$

where α is the linear absorption coefficient, υ is the frequency of the electromagnetic wave, A is constant and varies for different transitions, and n is equal to 1/2 for direct band gap. The graphs of $(\alpha\upsilon)^2$ vs υ were plotted for all three samples (Fig. 6). The extrapolation of the linear part to the υ axis determines the magnitude of E_g. The specified E_g magnitudes are equal 1.291, 1.302, and 1.312 eV for $x = 0.0$, 0.2, and 0.3, respectively. A remarkable increase

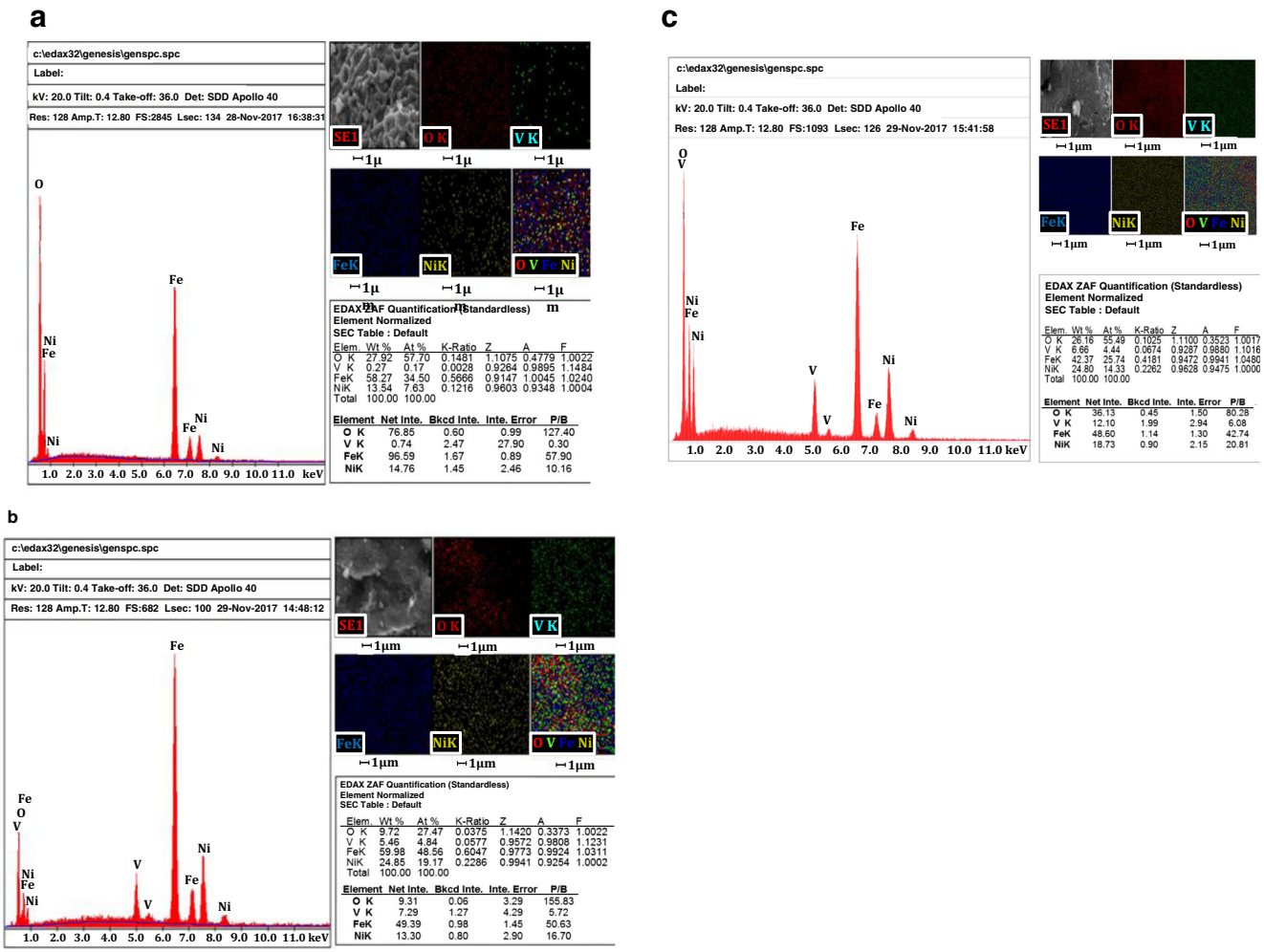

Fig. 4 EDX spectra and elemental mapping image of $NiFe_{2-x}V_xO_4$ NPs. **a** $x = 0.0$. **b** $x = 0.2$. **c** $x = 0.3$

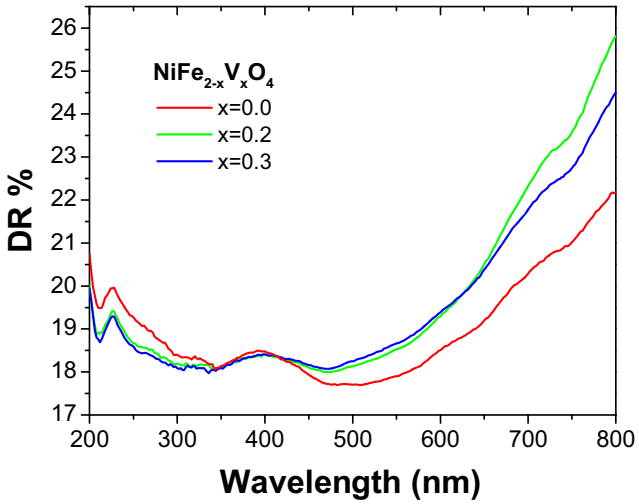

Fig. 5 %DR spectra of $NiFe_{2-x}V_xO_4$ ($x \leq 0.3$) NPs

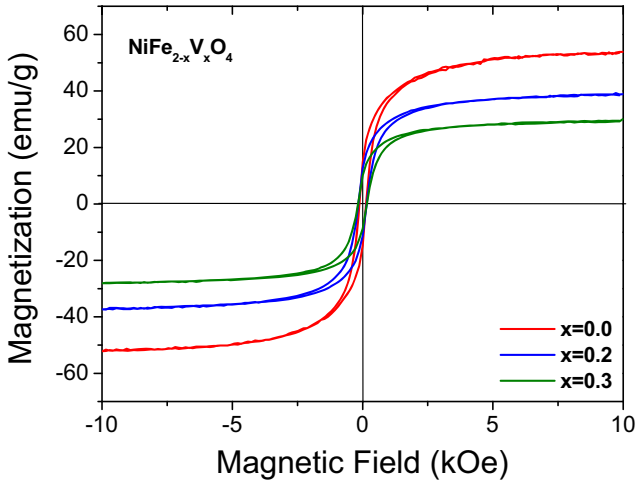

Fig. 7 Magnetization curves of $NiFe_{2-x}V_xO_4$ ($x \leq 0.3$) NPs

of E_g was detected for both doped samples with respect to the band gap of pristine $NiFe_2O_4$. In the literature, no report about the E_g values based on %DR investigations for $NiFe_{2-x}V_xO_4$ ($x \leq 0.3$) NPs is determined. The increasing quantum confinement size effect due to decreasing particle (or grain) dimensions might be assigned as the reason for a slightly higher magnitude of E_g for vanadium ion-doped NPs.

3.5 Magnetization Measurements

Magnetization vs magnetic field (σ-H) hysteresis curves of $NiFe_{2-x}V_xO_4$ ($x \leq 0.3$) NPs are displayed in Fig. 7. The σH curves were performed by the VSM device at 300 K with an externally applied field up to ± 10.0 kOe. The maximum magnetization corresponding to $H =$

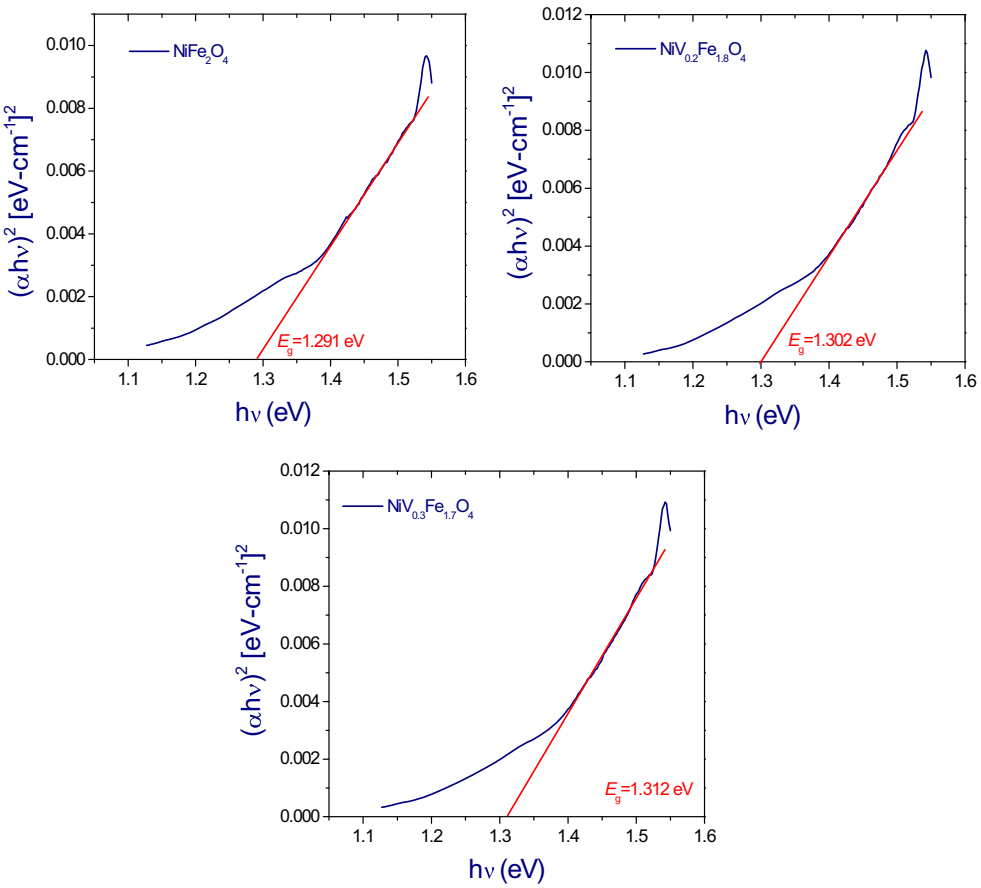

Fig. 6 $[F(R)\upsilon]^2$ against photon energy (υ) plots for $NiFe_{2-x}V_xO_4$ ($x \leq 0.3$) NPs. A regression line to the υ axis specifies the E_g

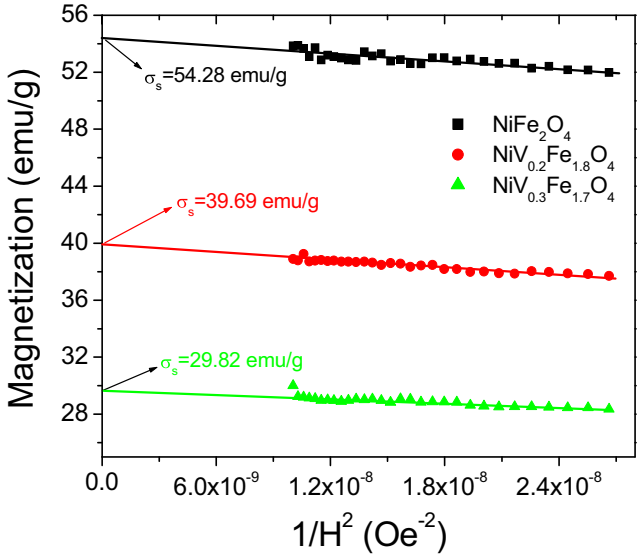

Fig. 8 Plots of M against $1 / H^2$ for $NiFe_{2-x}V_xO_4$ ($x \leq 0.3$) NPs

10.0 kOe is 53.86 emu/g and corresponds to $NiFe_2O_4$ product ($x = 0.0$). V^{3+} coordination causes remarkable decrements at corresponding magnetizations. The saturation magnetization (σ_s) was specified by the Stoner-Wohlfarth (S-W) theory by extrapolating the plot of σ vs $1 / H^2$ to approach zero [30–32]. The plots σ vs $1 / H^2$ for $NiFe_{2-x}V_xO_4$ ($x \leq 0.3$) NPs are presented with saturation magnetization values in Fig. 8. Magnetic hysteresis curves registered from all NPs have coercive fields (H_c) in the 125–169 Oe range and remanent magnetizations (σ_r) in the 9.36–14.04 emu/g range. Hence, we can say that all pristine and V^{3+}-doped samples exhibit a ferrimagnetic behavior at room temperature. All corresponding magnetizations (σ) for 10 kOe; molecular weights (H_c); σ_r, σ_s, and σ_r/σ_s ratios; and n_B values which depend on vanadium ion content are listed in Table 2.

The experimental magnetic moments per formula in the unit of Bohr magnetons (μ_B) were estimated using the expression, n_B= (Molecularweight×σ_s)/5585. Inverse spinel structured $NiFe_2O_4$ ferrite is found to have theoretical values of $n_B = 2\mu_B$ and σ_s= 50emu/g at 293 K [33, 34]. However, $NiFe_2O_4$ NPs in our study have larger experimental σ_s and n_B values. The values of σ_s are very comparable to those deduced from the $\sigma(H)$ loops in $H = \pm$ 10 kOe. The highest value of σ_s, about 54.28 emu/g, belongs to the pristine sample. With increasing V^{3+} content, σ_s decreases. A similar trend has been observed for $CoFe_{2-x}V_xO_4$ and $CoFe_{2-1.67x}V_xO_4$ [35]. The reducing of σ_s is most probably ascribed to the weakening of exchange interactions because of the substitution of Fe^{3+} ions by V^{3+} ions and by the preferred site occupancy [36, 37]. The variations of σ_r display the same tendency of the one for σ_s. σ_r reaches the maximum for the pure one then shows a decrease as the V concentration increases. Similar results have been observed for other substituted spinel ferrites [35, 38]. The squareness ratio (σ_r/σ_s) takes approximate values of 0.83 and 0.50 for cubic and uniaxial anisotropy, respectively [28]. In our study, σ_r/σ_s ratios are lower than 0.50, suggesting the uniaxial anisotropy for $NiFe_{2-x}V_xO_4$ NPs instead of expected cubic anisotropy [28].

In Fig. 8, the slope of linear fit provides a constant b value which is associated with the magnetocrystalline anisotropy in addition to extrapolated σ_s magnitudes. The expression that relates σ and the constant b is given, for high enough fields, by (2)

$$\sigma = \sigma_s \left(1 - \frac{b}{H^2}\right) \tag{2}$$

The effective anisotropy constant (K_{eff}) can be evaluated as [39]

$$K_{eff} = \sigma_s \left(\frac{15b}{4}\right)^{0.5} \tag{3}$$

The evaluated K_{eff} values enable us to calculate the anisotropy field (H_a). The expression which depends on K_{eff} and σ_s is

$$H_a = \frac{2K_{eff}}{\sigma_s} \tag{4}$$

The coercive field equation for non-interacting single-domain NPs is expressed as

$$H_c = 0.48\left[\left(\frac{2K_{eff}}{\mu_0 \sigma_s}\right) - N\sigma_s\right] \tag{5}$$

where N is the demagnetizing factor. We used this equation to calculate the demagnetizing factors of $NiFe_{2-x}V_xO_4$ ($x \leq 0.3$) NPs. The magnitudes of b constants N, H_a, and K_{eff} for all NPs are given in Table 3.

The value of K_{eff} for the pure $NiFe_2O_4$ was found to be 1.30 ×10^5 Erg/g. Then, K_{eff} decreases as the V content increases. This is ascribed to the replacement of Fe^{3+} ions by V^{3+} ions. The coercive fields (σ_c) obtained in our study (Table 2) are greatly altered by the V content. As

Table 2 Molecular weight and magnetic properties of $NiFe_{2-x}V_xO_4$ ($x \leq 0.3$) NPs

x	Molecular weight	H_c (Oe)	σ (emu/g)	σ_r (emu/g)	σ_s (emu/g)	σ_r/σ_s	$n_B\mu_B$)
0.0	234.38	125	53.86	14.04	54.28	0.25	2.2
0.2	233.40	154	38.90	11.51	39.69	0.29	1.6
0.3	232.92	169	29.83	9.36	30.82	0.30	1.2

Table 3 V content (x), b, K_{eff}, H_a, and N values for $NiFe_{2-x}V_xO_4$ ($x \leq 0.3$) NPs

x	b (Oe^2)	K_{eff} (Erg/g)	H_a (Oe)	N (Oe^2/g/Erg)
0.0	1.537×10^6	1.303×10^5	4802	83.65
0.2	1.952×10^6	1.074×10^5	5412	128.27
0.3	1.908×10^6	0.824×10^5	5349	162.07

the V^{3+} amount increases, σ_c increases too, designating that the non-magnetic V^{3+} ions are very effective in the increase of σ_c. This is mostly derived from the reduction of magnetocrystalline anisotropy effect and crystallite size [40–43]. In our study, XRD results show a reduction of crystallite sizes with the increasing V content. Furthermore, it is clear that the effective anisotropy constant is also decreased with regard to V^{3+}. These two reasons prove the enhancement of σ_c in the current study. When σ_c augments, a strong demagnetizing field is required to surpass the magnetocrystalline anisotropy energy barrier. This is in agreement with the obtained values of N, which increase from 83.65 Oe^2/g/Erg for the pristine NPs to 162.07 Oe^2/g/Erg for $x = 0.3$. Another reason of the improvement of σ_c is the rising of anisotropy field (H_a) [36]. In our study, the values of H_a are smaller (around 5 kOe), proving that all

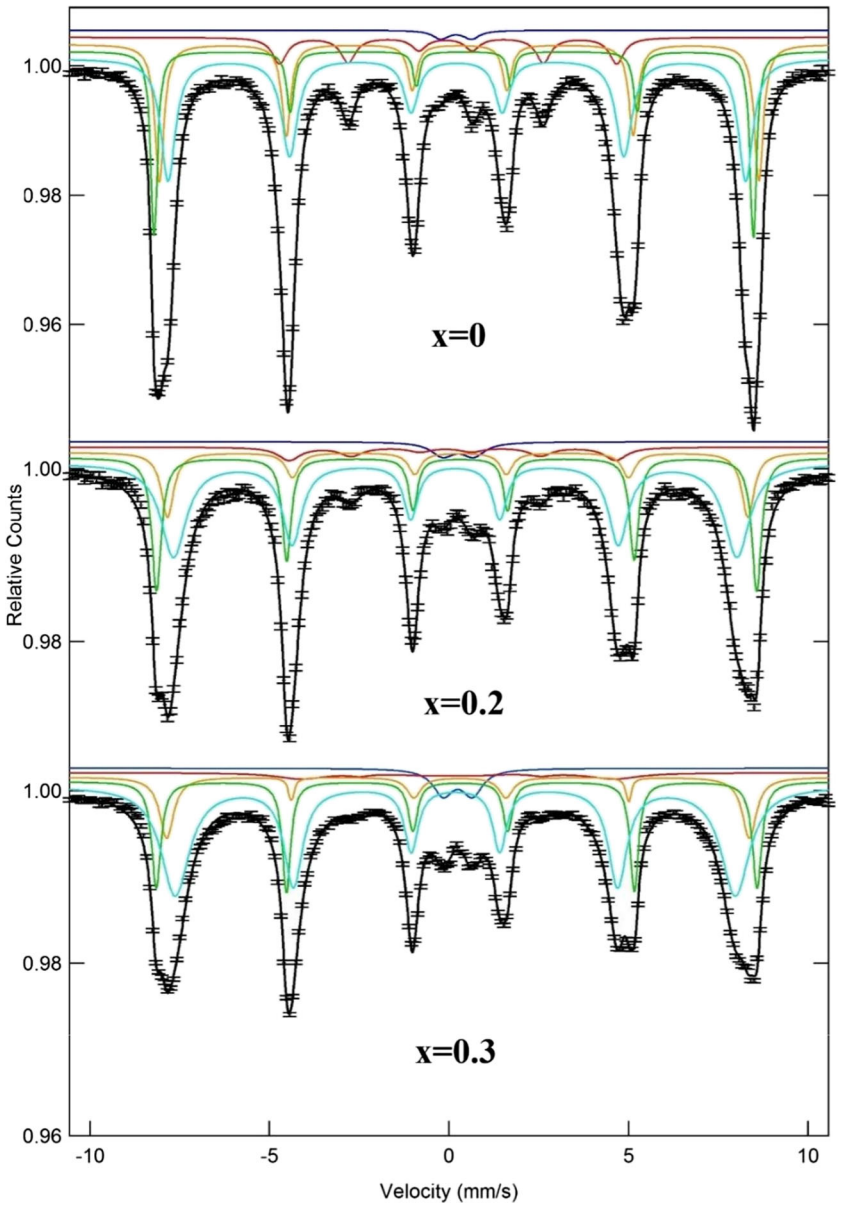

Fig. 9 Mossbauer spectra of $NiFe_{2-x}V_xO_4$ ($x \leq 0.3$) NPs a

Table 4 Mossbauer parameters for $NiFe_{2-x}V_xO_4$ ($x \leq 0.3$) NPs

x	Assignment of sites	IS (± 0.002) (mm/s)	QS (± 0.004) (mm/s)	B_{hf} (± 0.05) (T)	W (± 0.04) (mm/s)	RA (%)	Cation distribution
0.0	Sx = A: Fe^{3+}	0.375	− 0.274	51.687	0.236	13.863	$(Ni_{0.72}Fe_{0.28})_A[Ni_{0.28}Fe_{1.72}]_BO_4$
	Sx = B: Fe^{3+}	0.391	− 0.007	51.681	0.319	20.819	
	Sx = B_1: Fe^{3+}	0.321	0.006	49.778	0.479	48.311	
	Sx = B_2: Fe^{3+}	0.088	0.128	29.15	0.549	15.268	
	Db: Fe^{3+}	0.325	0.86	–	0.438	1.7394	
0.2	Sx = A: Fe^{3+}	0.371	− 0.106	51.799	0.297	18.387	$(Ni_{0.65}Fe_{0.35})_A[Ni_{0.35}V_{0.2}Fe_{1.45}]_BO_4$
	Sx = B: Fe^{3+}	0.388	− 0.079	50.102	0.415	13.452	
	Sx = B_1: Fe^{3+}	0.281	0	48.635	0.484	53.202	
	Sx = B_2: Fe^{3+}	0.113	0.188	28.191	0.727	9.4822	
	Db: Fe^{3+}	0.364	0.854	–	0.763	5.1946	
0.3	Sx = A: Fe^{3+}	0.372	− 0.102	51.857	0.311	14.31	$(Ni_{0.74}Fe_{0.26})_A[Ni_{0.24}V_{0.3}Fe_{1.44}]_BO_4$
	Sx = B: Fe^{3+}	0.385	− 0.054	50.293	0.471	11.658	
	Sx = B_1: Fe^{3+}	0.28	− 0.006	48.349	0.467	53.155	
	Sx = B_2: Fe^{3+}	0.253	0.205	27.064	1.642	14.033	
	Db: Fe^{3+}	0.355	0.814	–	0.742	6.8434	

IS isomer shift, *QS* quadrupole splitting, B_{hf} hyperfine magnetic field, *W* line width, *RA* relative area

obtained NPs are magnetically soft. Moreover, H_a increases with rising V amount, which confirms the enhancement of σ_c values with regard to V^{3+}.

3.6 Mossbauer Study and Cation Distribution Calculation

The Mossbauer spectra of $NiFe_{2-x}V_xO_4$ ($x \leq 0.3$) NPs are depicted in Fig. 9. Different parameters estimated from the fitting of these spectra are presented in Table 4. One doublet and four sextets were used for the fitting procedure; A is considered for the T_d sites while B, B_1, and B_2 correspond to the O_h sites. The highest hyperfine field (B_{hf}) with lower isomer shift (IS) is characteristic of Fe^{3+} ions in the T_d site; however, the other three sextets with relatively smaller hyperfine field represent Fe^{3+} ions at three different environments in B site [44, 45]. The relative area (RA) of A and B sites from obtained Mössbauer spectroscopy indicates that the Ni ions are located in A and B sites. According to Shannon, V^{3+} (0.78 Å) prefers to occupy the O_h sites [46]. Therefore, the cation distribution of $NiFe_{2-x}V_xO_4$ was done using the formula $(Ni_yFe_{1-y})^A(Ni_{1-y}V_xFe_{1+y-x})^B$. The RA of Fe^{3+} ions is occupied by T_d and O_h sites. The distribution of Fe^{3+} ions over A and B sites is proportional to the RA of A and B Mossbauer sub-spectra. The calculated cation distribution from Mossbauer spectroscopy is also given in Table 4. According to Table 4, Fe^{3+} cations emigrated from B to A site with substitution. Also, the Mossbauer spectral area of doublet increases linearly as the V amount increases. The IS values vary between 0.088 and 0.391 mm/s. Such values are associated to the characteristic high-spin Fe^{3+} charge state [47]. While the IS value of A, B, and B_1 sites decreases continuously, it increases in the B_2 site with the increase of x. These show that the electron density around iron in all sites was affected by the substitution. The value of quadrupole splitting (QS) of B_2 site continuously increases with the increase of x. This shows that the B_2 site is deviated from cubic symmetry with the substitution. The value of B_{hf} at A site is nearly constant, while in the other sites, it shows a decrease with the substitution. The decrease of B_{hf} at B site may be ascribed to the weakening of A-B superexchange interactions owing to the presence of V^{3+} ions at the B site.

4 Conclusion

$NiFe_{2-x}V_xO_4$ ($x \leq 0.3$) NPs were produced using the sol-gel route. The XRD analyses established the fabrication of a specific product for each substitution. The porous morphology with the average grain size of 150 nm was observed by HR-SEM analysis. The E_g values increase from 1.291 to 1.312 eV due to the slightly decreasing

particle size caused by the vanadium ion substitution. The pristine $NiFe_2O_4$ NPs have stronger $\sigma_s = 53.86$ emu/g and $n_B = 2.2\ \mu_B$ values than the theoretical ones. However, anisotropy fields around 5 kOe with the corresponding low coercive fields in a 125–169-Oe interval and the remanent magnetizations in the 9.36–14.04 emu/g range revealed the soft ferrimagnetic nature of $NiFe_{2-x}V_xO_4$ ($x \leq 0.3$) NPs. σ_r/σ_s ratios less than 0.500 suggest the uniaxial anisotropy for as-prepared ceramic powders. From Mössbauer analysis, the cation distribution of $NiFe_{2-x}V_xO_4$ products was done by means of the formula $(Ni_yFe_{1-y})^A(Ni_{1-y}V_xFe_{1+yx})^B$.

Funding Information Prof. A. Baykal and Dr. Y. Slimani thank the Deanship of Scientific Research (DSR) and the Institute for Research and Medical Consultations (IRMC) of Imam Abdulrahman Bin Faisal University for the support through the project application numbers 2017-605-IRMC and 2018-209-IRMC.

References

1. Sloczynski, J., Janas, J., Machej, T., Rynkowski, J., Stoch, J.: Appl. Catal. B. **24**, 45–60 (2000)
2. Almessiere, M.A., Dabagh, S., Slimani, Y., Chaudhary, K., Ali, J., Baykal A.: Journal of Inorganic and Organometallic Polymers and Materials. https://doi.org/10.1007/s10904-017-0764-9 (2018)
3. Koledintseva, M., Drewniak, J., Zhang, Y., Lenn, J., Thoms, M.: J. Magn. Magn. Mater. **321**, 730–733 (2009)
4. Amir, Md., Gungunes, H., Slimani, Y., Tashkandi, N., El Sayed, H.S., Aldakheel, F., Sertkol, M., Sozeri, H., Manikandan, A., Ercan, I., Baykal, A.: J. Supercond. Nov. Magn. https://doi.org/10.1007/s10948-018-4733-5 (2018)
5. Cao, S.W., Zhu, Y.J., Cheng, G.F.: J. Hazard. Mater. **171**, 431–435 (2009)
6. Yadav, R.S., Kuritka, I., Havlica, J., Hnatko, M., Alexander, C., Masilko, J., Kalina, L., Hajdúchová, M., Rusnak, J., Enev, V.: J. Magn. Magn. Mater. **447**, 48–57 (2018)
7. Blasse, G.: Philips Tech. Rev. **28**, 23–30 (1967)
8. Lahiri, P., Sengupta, S.K.: J. Chem. Soc., Faraday Trans. **91**, 3489–3494 (1995)
9. Joshi, S., Kumar, M., Chhoker, S., Srivastava, G., Jewariya, M., Singh, V.N.: J. Mol. Struct. **1076**, 55–62 (2014)
10. Larumbe, S., Gómez-Polo, C., Pérez-Landazábal, J., García-Prieto, A., Alonso, J., Fdez-Gubieda, M.L., Cordero, D., Gómez, J.: J. Nanosci. Nanotechnol. **12**, 2652–2660 (2012)
11. Chinnasamy, C.N., Narayanasamy, A., Ponpandian, N., Chattopadhyay, K., Shinoda, K., Jeyadevan, B., Tohji, K., Nakatsuka, K., Furubayashi, T., Nakatani, I.: Phys. Rev. B **63**, 184108 (2001)
12. Iranmanesh, P., Tabatabai Yazdi, S.h., Mehran, M., Saeednia, S.: J. Magn. Magn. Mater. **449**, 172–179 (2018)
13. Lüders, U., Herranz, G., Bibes, M., Bouzehouane, K., Jacquet, E., Contour, J.-P., Fusil, S., Bobo, J.F., Fontcuberta, J.: J. Appl. Phys. **99**, 08K301 (2006)
14. Kwon, W.H., Lee, J.-G., Lee, S.W., Chae, K.P.: J. Korean Phys. Soc. **56**, 1838–1842 (2010)
15. Heiba, Z.K., Mohamed, M.B., Ahmed, S.I.: J. Magn. Magn. Mater. **441**, 409–416 (2017)
16. Maisnam, M., Phanjoubam, S., Sarma, H.N.K., Devi, L.R., Thakur, O.P., Prakash, C.: Physica B **352**, 86 (2004)
17. Chae, K.P., Kwon, W.H., Lee, J.G.: J. Magn. **15**, 25–28 (2010)
18. Maisnam, M., Phanjoubam, S., Sarma, H.N.K., Prakash, C., Devi, L.R., Thakur, O.P.: Mater. Lett. **58**, 2412–2414 (2004)
19. Jain, G., Das, B., Tripathi, R., Narayan, R.: IEEE Trans. Magn. **18**, 776–778 (1982)
20. Baykal, A., Eryiğit, Ş., Topkaya, R., Güngüneş, H., Amir, Md., Yıldız, A., Kurtan, U., Shirsath, S.E.: Ceramics Int. **43**, 4746–4752 (2017)
21. Maisnam, M., Phanjoubam, S., Sarma, H.N.K., Prakash, C., Devi, L.R., Thakur, O.P.: Mater. Lett. **58**, 2412–2414 (2004)
22. Wejrzanowski, T., Pielaszek, R., Opalinska, A., Matysiak, M., Lojkowski, W., Kurzydlowski, K.J.: Appl. Surf. Sci. **253**, 204 (2006)
23. Pielaszek, R.: Proceedings of the XIX Applied Crystallography Conference, p. 43. Krakow (2003)
24. Vadivel, M., Ramesh Babu, R., Sethuraman, K., Ramamurthi, K., Arivanandhan, M.: J. Magn. Magn. Mater. **362**, 122–129 (2014)
25. Jauhar, S., Singhal, S.: Ceram. Int. **40**, 11845–11855 (2014)
26. Kaiser, M.: J. Phys. Chem. Solids **71**, 1451–1457 (2010)
27. Slimani, Y., Güngüneş, H., Nawaz, M., Manikandan, A., El Sayed, H.S., Almessiere, M.A., Sözeri, H., Shirsath, S.E., Ercan, I., Baykal, A.: Ceram. Int. **44**, 14242–14250 (2018)
28. Stoner, E.C., Wohlfarth, E.P.: Phil. Trans. R. Soc. A **240**, 599–642 (1948)
29. Kojima, H., Wohlfarth, E.P.: Ferromagnetic Materials, vol. 3, p. 305. North-magneto-optical recording, Amsterdam (1982)
30. Almessiere, M.A., Slimani, Y., Baykal, A.: Ceram. Int. **44**, 9000–9008 (2018)
31. Almessiere, M.A., Slimani, Y., Baykal, A.: J. Alloys Compd. **762**, 389–397 (2018)
32. Almessiere, M.A., Slimani, Y., El Sayed, H.S., Baykal, A.: Ceram. Int. **44**, 12511–12519 (2018)
33. Cullity, B.D., Graham, C.D.: Introduction to Magnetic Materials. Wiley, Hoboken (2008)
34. Kavas, H., Baykal, A., Toprak, M.S., Koseoglu, Y., Sertkol, M., Aktaş, B.: J. Alloys Compd. **479**, 49–55 (2009)
35. Heiba, Z.K., Mohamed, M.B., Ahmed, S.I.: J. Magn. Magn. Mater. **441**, 409–416 (2017)
36. Shams, M.H., Rozatian, A.S., Yousefi, M.H., Valícek, J., Sepelak, V.: J. Magn. Magn. Mater. **399**, 10–18 (2016)
37. Topkaya, R., Auwal, I., Baykal, A.: Ceram. Int. **42**, 16296–16302 (2016)
38. Toksha, B.G., Shirsath, S.E., Mane, M.L., Patange, S.M., Jadhav, S.S., Jadhav, K.M.: J. Phys. Chem. C **115**, 20905–20912 (2011)
39. Amir, Md., Geleri, M., Güner, S., Baykal, A., Sözeri, H.: J. Inorg. Organomet. Polym. Mater. **25**, 1111–1119 (2015)
40. Cao, C., Li, X., Luo, B., Li, Y., Zhang, A., Xia, A.: J. Supercond. Nov. Magn. (2017), https://doi.org/10.1007/s10948-017-4314-z
41. Mirkazemi, S.M., Alamolhoda, S., Ghiami, Z.: J. Supercond. Nov. Magn. **28**, 1551–1558 (2015)
42. Li, X., Sun, R., Luo, B.Y., Zhang, A.J., Xia, A.L., Jin, C.G.: J. Mater. Sci. Mater. Electron. **28**, 12268–12272 (2017)
43. Asiri, S., Güner, S., Korkmaz, A.D., Amir, Md., Batoo, K.M., Almessiere, M.A., Gungunes, H., Sözeri, H., Baykal, A.: J. Magn. Magn. Mater. **451**, 463–472 (2018)
44. Ayyappan, S., Philip Raja, S., Venkateswaran, C., Philip, J., Raj, B.: Appl. Phys. Lett. **96**, 143106–143109 (2010)
45. Joseyphus, R.J., Narayanasamy, A., Shinoda, K., Jeyadevan, B., Tohji, K.: J. Phys. Chem. Solids. **67**, 1510–1517 (2006)
46. Shannon, R.D.: Acta Crystallogr. Sect. A: Found. Crystallogr. A **32**, 751–767 (1976)
47. Sorescu, M., Diamandescu, L., Peelamedu, R., Roy, R., Yadoji, P.: J. Magn. Magn. Mater. **279**, 195–201 (2004)